Research article

A comparative X-ray diffraction analysis of Sr^{2+} substituted hydroxyapatite from sand lobster shell waste using various methods

Arian Hermawan Diputra , I Kadek Hariscandra Dinatha , Yusril Yusuf [*]

Department of Physics, Faculty of Mathematics and Natural Sciences, Universitas Gadjah Mada, Yogyakarta, 55281, Indonesia

ARTICLE INFO

ABSTRACT

This study aims to investigate the crystallographic properties of hydroxyapatite (HAp) and strontium-substituted hydroxyapatite (SrHAp) obtained from sand lobster shells (SLS) using various analytical methods. HAp and SrHAp were synthesized by the hydrothermal method using sand lobster (*Panulirus homarus*) shell waste as a calcium precursor. SLS were calcined at 0 °C, 600 °C, 800 °C, and 1000 °C and characterized by X-ray diffraction (XRD). HAp and SrHAp were analyzed by XRD and transmission electron microscopy (TEM). XRD results revealed that SLS calcined at 1000 °C displayed a Ca(OH)2 phase, while those calcined at other temperatures showed a CaCO3 phase. The characterization also verified the diffraction patterns of HAp and SrHAp according to the reference model. Various methods, including the Scherrer method, linear straight-line Scherrer method, Monshi-Scherrer method, Williamson-Hall plot, size-strain plot, and Halder-Wagner method, were employed to investigate the microstructure parameters (crystallite size and microstrain). All methods resulted in varied yet comparable results of crystallite size, except for the linear straight-line Scherrer method. The TEM results showed that the particle sizes of HAp and SrHAp were approximately 130 nm. In this study, the W-H plot was regarded as the best method for providing additional information on anisotropy elasticity and consistent crystallite size results.

1. Introduction

The growing interest in biomaterials has driven significant research efforts in recent years, particularly in the field of bone tissue engineering. Hydroxyapatite ($Ca_{10}(PO_4)_6(OH)_2$, HAp) has garnered attention due to its chemical similarity to human bone [1], making it a promising candidate for biomedical applications [2–4]. A variety of methods have been established for HAp synthesis, such as sol-gel [5], wet chemical precipitation [6], and hydrothermal [7]. HAp can be synthesized from either synthetic materials or natural sources. Many studies have reported the compatibility of natural sources in synthesizing HAp, such as eggshells [8], mammalian bones [9,10], and marine sources [11]. We utilized sand lobster (*Panulirus homarus*) shell waste as a calcium precursor for HAp synthesis using the hydrothermal method. The sand lobster shells (SLS) are continuously available due to the periodic molting cycle of the lobsters [12,13]. Various modifications, such as substituting metal ions like the Sr^{2+}, Mg^{2+}, and CO_3^{2-} [14], have been employed to enhance the physicochemical, mechanical, and biological properties of HAp. The substitution of Sr^{2+} has been shown to enhance the

---

* Corresponding author.
 E-mail address: yusril@ugm.ac.id (Y. Yusuf).

biological properties of HAp in bone remodeling [15]. Furthermore, Sr-doped CaP bioceramics have been demonstrated to promote bone regeneration [16,17].

X-ray diffraction (XRD) analysis has been widely used to characterize materials in terms of crystallographic properties, such as crystallite size, crystallinity, and microstrain. In search of a perfect crystal, one would expect it to extend infinitely in all directions. However, no crystals are perfect due to their finite size. This imperfection in crystal structure results in the broadening of diffraction peaks [18]. The broadening of XRD peaks is primarily influenced by lattice strain and crystal size. Intrinsic strain in the crystal generally arises from the large grain boundary areas and the inherent imperfections in crystalline materials [19,20]. Generally, Scherrer's equation is used to estimate the crystallite size of materials depending on the width of the XRD peaks. However, this method neglects the contribution of intrinsic strain and instrumental effects that influence the peak broadening. Therefore, X-ray peak profile analysis (XPPA) considers these peak broadening contributions to estimate the microstructural properties of materials, mainly crystallite size and microstrain [21,22]. Some methods of this XPPA are the Scherrer method, the Monshi-Scherrer method, the linear straight-line Scherrer method, the Williamson-Hall (W-H) plot, the size-strain plot (SSP), and the Halder-Wagner (HW) method. The Monshi-Scherrer method is also called the modified Scherrer equation and was found in 2012 by Monshi et al. [23], which gave a correction to the standard Scherrer's equation. The W-H method consists of the uniform deformation model (UDM), uniform stress deformation model (USDM), and uniform deformation energy density model (UDEDM), which provide a calculation of elastic properties, such as Young's modulus, stress, and energy density. These methods also consider the anisotropic elasticity of materials [24,25]. The SSP method regards the XRD peak broadening which consists of the size-widened component as the Lorentzian function and the strain-broadened component as the Gaussian function [26,27]. This method has the advantage of providing more precise results by giving less weight to data from reflections at high angles, where accuracy is typically poorer [28]. In contrast, the HW method
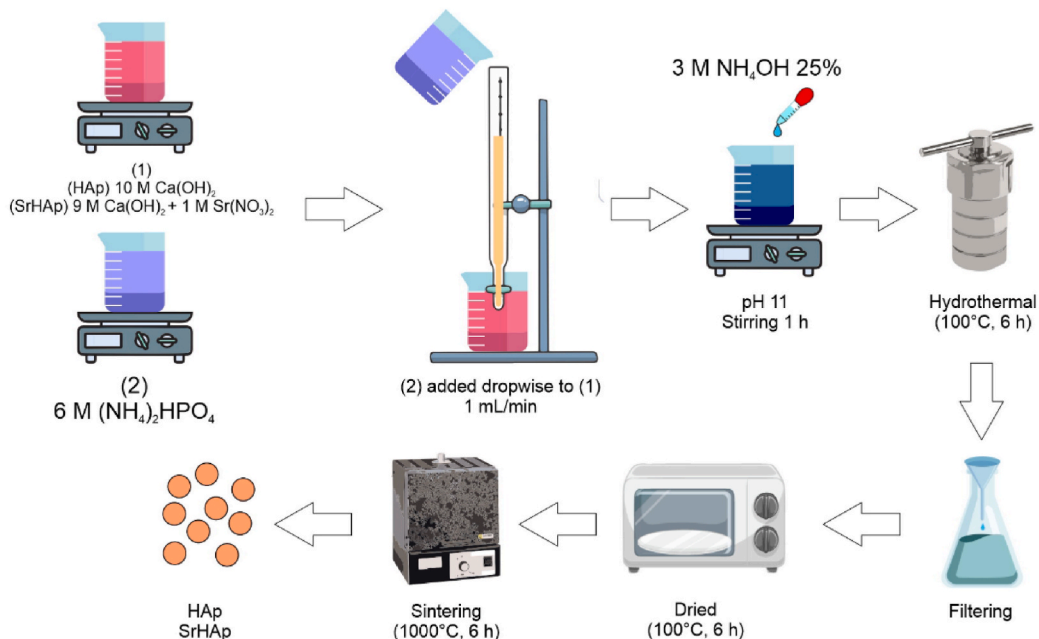

Fig. 1. Schematic methods of (a) preparation of SLS and (b) synthesis of HAp and SrHAp.

interprets the peak broadening as a Voigt function, which assumes that typical strain and size can be inferred from the widening of the XRD peaks [29]. Hence, the authors were inspired to apply these methods to investigate the crystallographic properties of HAp and strontium-substituted hydroxyapatite (SrHAp) derived from SLS. To the best of our knowledge, no existing reports cover this specific investigation.

In this study, a comparative X-ray profile analysis of HAp and SrHAp derived from SLS waste by using Scherrer method, linear straight-line Scherrer method, Monshi-Scherrer method, Williamson-Hall plot, size-strain plot, and Halder-Wagner method was reported. In addition, transmission electron microscopy (TEM) has been used to examine the shape and particle size of the HAp and SrHAp.

2. Materials and methods

2.1. Materials

Sand lobster shells were obtained from Buleleng, Bali, Indonesia as a calcium source. Diammonium hydrogen phosphate ($(NH_4)_2HPO_4$), strontium nitrate $Sr(NO_3)_2$, and ammonium hydroxide (NH_4OH) were purchased from Merck (USA).

2.2. Extraction of sand lobster shells

Sand lobster shells were cleaned and washed using water before drying in the oven (Memmert, UN55, Germany) at 100 ° C for 6 h. The shells were then ground into a fine powder using a ball mill (Kawasaki, T-100, Kobe, Japan). The powder was calcined at 600 °C, 800 °C, and 1000 °C using a furnace (Vulcan A-130, USA) with a heating rate of 32 °C/min under atmospheric conditions. The chemical reaction for the extraction of sand lobster shells is shown in Equation (1). The samples were designated as SLS_0, SLS_600, SLS_800, and SLS_1000.

$$CaCO_3 \text{ (s)} \xrightarrow{1000°C} CaO \text{ (s)} + CO_2 \text{ (g)} \tag{1}$$

2.3. Synthesis of HAp and SrHAp

Based on our previous studies [30,31], the SLS_1000 ($Ca(OH)_2$) sample is the best candidate as a calcium source to synthesize HAp. To synthesize HAp, 10 M $Ca(OH)_2$ and 6 M $(NH_4)_2HPO_4$ were dissolved in 70 mL of deionized water. The $(NH_4)_2HPO_4$ solution was added dropwise to the $Ca(OH)_2$ solution at a rate of 1 mL/min. A 3M NH_4OH 25 % solution was added to control the pH to 11 and maintained with constant stirring for 1 h until homogeneous. The mixed solution was then transferred to an autoclave and heated at 100 ° C in an oven for 6 h. The solution was filtered, washed, and dried at 100 ° C for 6 h. The obtained HAp powder was sintered at 1000 ° C for 6 h. The SrHAp synthesis followed the same process. However, the composition of $Ca(OH)_2$ was altered to 9 M $Ca(OH)_2$ and 1 M $Sr(NO_3)_2$. The schematic procedure is illustrated in Fig. 1.

2.4. Characterization

Crystallographic properties of the samples were characterized by X-ray diffraction analysis (XRD, Bruker D8 Advance, USA). The XRD analysis was carried out at 40 kV and 30 mA. The diffraction pattern was recorded in the range of 2 θ from 10 ° to 70 ° using K α_1 radiation (λ = 1.5406 Å). To analyze the particle size of the HAp and SrHAp, transmission electron microscopy (TEM, Jeol JEM-1400, Japan) was used. The crystallographic properties of the samples were calculated using Equation (2) – Equation (5).

$$\text{Lattice parameters}, \frac{1}{d_{hkl}{}^2} = \frac{4}{3}\left(\frac{h^2 + hk + k^2}{a^2}\right) + \frac{l^2}{c^2} \tag{2}$$

$$\text{Cell volume}, V = \frac{\sqrt{3}}{2}a^2 c \tag{3}$$

$$\text{Microstrain}, \varepsilon = \frac{\beta}{4 \tan \theta} \tag{4}$$

$$\text{Crystallinity index}, CI = \left(1 - \frac{V_{112/300}}{I_{300}}\right) \times 100\% \tag{5}$$

$$\text{Density}, \rho = \frac{n \cdot M}{N_A \cdot V} \tag{6}$$

Where d_{hkl} is inter-atomic spacing; h, k, l are Miller indices; a, b, c are lattice parameters; V is cell volume; ε is microstrain; β is full-width at half maximum (FWHM); and θ is diffraction angle. The crystallinity index and density were applied to HAp and SrHAp, where $V_{112/300}$ is the intensity of the valley between the diffraction planes of (112) and (300); I_{300} is the intensity of the (300) diffraction plane

[32]; n is the effective number of atoms per unit cell (for HAp = 1); M is the molar mass; and N_A is Avogadro's number (6.022×10^{23} mol^{-1}).

3. Results and discussion

3.1. XRD crystallographic analysis

The X-ray diffraction (XRD) analysis of SLS (Fig. 2) showed that the samples calcined at 0 ° C, 600 ° C, and 800 ° C primarily presented a CaCO$_3$ phase. The peaks at 22.8 °, 29.2 °, 35.8 °, 39.2 °, 43.0 °, 47.3 °, and 48.3 ° corresponded to the diffraction planes (012), (104), (110), (113), (202), (024), and (116), respectively [33]. At 1000 ° C, SLS decomposed from CaCO$_3$ to CaO, as shown in Equation (1). However, the observed peaks corresponded mostly to the Ca(OH)$_2$ rather than the CaO phase. The Ca(OH)$_2$ phase in SLS_1000 was verified by the peaks at 17.8 °, 28.6 °, 34.0 °, 47.0 °, 50.7 °, and 54.2 °, corresponding to the diffraction planes of (001), (100), (101), (102), (110), and (111), respectively [34]. This phase conversion to Ca(OH)$_2$ phase occurred because CaO is highly reactive to water vapor under atmospheric conditions, resulting in the interaction between CaO and H$_2$O Equation (7) [35,36].

$$CaO\ (s) + H_2O\ (g) \rightarrow CaOH_2\ (s) \tag{7}$$

From the XRD data, crystallographic properties such as lattice parameters, cell volume, and microstrain were calculated using Equation (2) – Equation (4) and are presented in Table 1. These results are crucial for determining the crystal structure of the samples. The crystal system and space group of the SLS_0, SLS_600, and SLS_800 were identified as trigonal and R-3c, respectively. Their lattice parameters were similar to the lattice parameters reference values (JCPDS No. 47–1743) of CaCO$_3$ (calcite), which are $a = b = 4.98$ Å and $c = 17.05$ Å. This also applied to the cell volume characteristic, which is 367.39 Å^3. The variations in calcination temperature influenced these values. At 800 ° C, SLS achieved a crystal structure closely related to the CaCO$_3$ phase. In addition to causing decomposition, the calcination process also promoted crystal growth, leading to an improved crystal structure. This phenomenon significantly influenced the untreated SLS, which had crystallographic values that deviated from the reference. Furthermore, the results also revealed that the untreated SLS contains a few impurities typically present in natural sources. In contrast, SLS_1000 exhibited the crystal structure of Ca(OH)$_2$ (portlandite), with lattice parameters of $a = b = 3.59$ Å and $c = 4.92$ Å and cell volume of 54.87 Å^3, which are in good agreement with the reference values (JCPDS No. 00-044-1481).
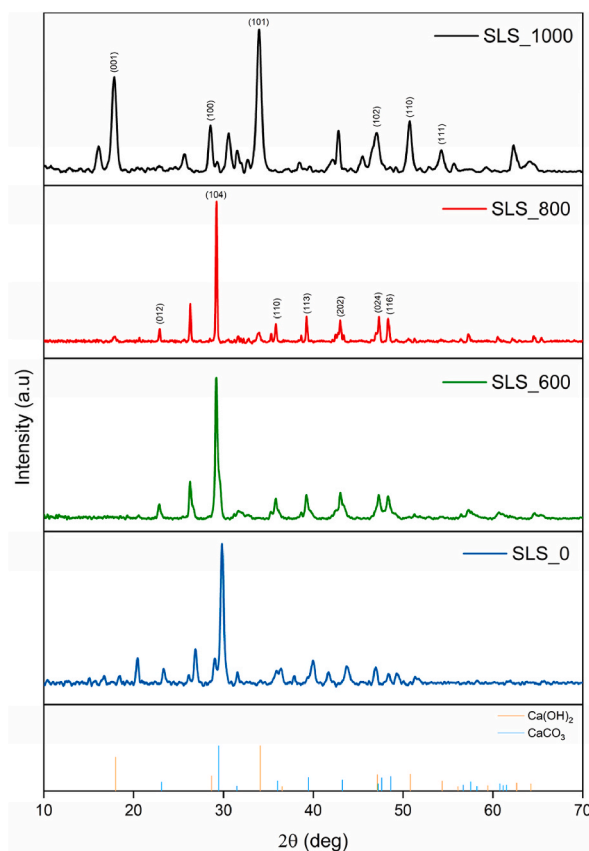

Fig. 2. XRD patterns of SLS_0, SLS_600, SLS_800, and SLS_1000.

Table 1
Crystallographic properties of SLS_0, SLS_600, SLS_800, and SLS_1000.

Parameter	Sample			
	SLS_0	SLS_600	SLS_800	SLS_1000
Lattice parameter (Å)	$a = b = 4.963$ $c = 16.66$	$a = b = 4.983$ $c = 17.29$	$a = b = 5.012$ $c = 17.18$	$a = b = 3.581$ $c = 4.96$
Cell volume (Å)	354.95	374.34	371.95	55.67
Microstrain, ε ($\times 10^{-3}$)	2.5	2.0	1.1	3.4

SLS_1000 was selected as the primary source of calcium for synthesizing HAp and SrHAp. XRD analysis (Fig. 3) revealed that the diffraction patterns of HAp and SrHAp predominantly showed a hydroxyapatite phase, with peaks at 25.7 °, 28.8 °, 31.6 °, 32.0 °, 32.7 °, 33.9 °, 39.6 °, 41.8°, 46.5 °, 47.9 °, 49.3 °, 50.3 °, 51.1 °, 51.9 °, and 53.1 °. These peaks corresponded to the diffraction planes (002), (210), (211), (112), (300), (202), (310), (311), (222), (312), (213), (321), (410), (402), and (004), respectively. The crystallographic properties (Table 2) were in good agreement with the reference values (JCPDS No. 09–0432), showing lattice parameters of $a = b = 9.4232$ Å and $c = 6.881$ Å, a cell volume of 529 Å^3, and a density of 3.05 g/cm^3 [37–39]. In SrHAp, deviations from these values were observed due to the addition of Sr^{2+}, which caused distortion in the hydroxyapatite crystal structure [40]. The distortion occurred because the ionic radius of Sr^{2+} (1.12 Å) is larger than that of Ca^{2+} (0.99 Å) Furthermore, the CI and microstrain results also indicated the distortion. The CI decreased with the addition of Sr^{2+}, and the microstrain was larger in SrHAp, suggesting that HAp had a more ordered structure compared to SrHAp. Despite this, the increase in lattice parameters in SrHAp confirmed that Sr^2 successfully substituted for Ca^{2+} in the hydroxyapatite structure [41]. Additionally, the diffraction peaks of SrHAp shifted to lower 2θ values (Table S6), leading to an increase in d-spacing and cell volume [42].

Fig. 4 shows the FWHM for various peaks of the diffraction patterns for SLS_0, SLS_600, SLS_800, HAp, and SrHAp. Since the SLS_1000 exhibited a Ca(OH)$_2$ phase, it was excluded from the analysis because of not sufficient variable to be compared. The decrease in FWHM observed with increasing calcination temperature in the SLS samples indicated enhanced crystallinity within the material. This trend suggests that higher calcination temperatures facilitate crystal growth, leading to larger crystallite sizes and improved atomic ordering. In addition, elevated temperatures likely relieve internal lattice strain, further narrowing the FWHM. The increase in FWHM observed in the SrHAp sample because the incorporation of Sr^{2+} leads to lattice distortion in the HAp crystal. Therefore, this increase in FWHM can lower the crystallite size and crystallinity of HAp.

Various methods have been developed for XRD analysis to determine crystallite size and other geometrical parameters, such as microstrain, stress, and energy density. These methods include the Scherrer method, Williamson-Hall plot, size-strain plot, and Halder-Wagner model, each of which is discussed below. The diffraction peaks evaluated using these methods are listed in Tables S1–6.

3.2. Average Scherrer method

The X-ray diffraction peak broadens due to the crystalline size effect and intrinsic strain. This broadening generally includes two components: physical broadening and instrumental broadening. Instrumental broadening can be corrected using Equation (8).
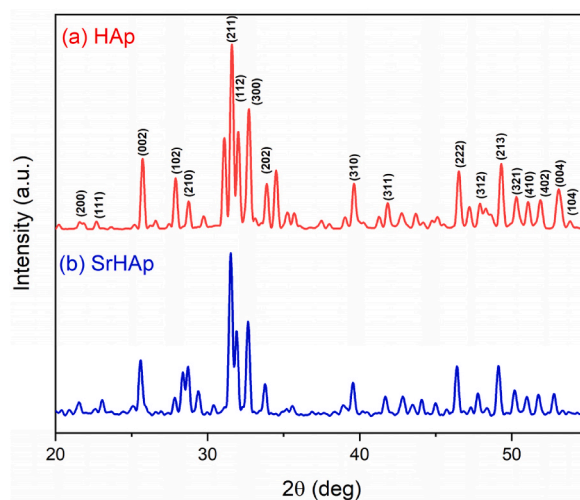
$$\beta_d{}^2 = \beta_m{}^2 + \beta_i{}^2 \tag{8}$$

Fig. 3. XRD patterns of HAp and SrHAp.

Table 2
Crystallographic properties of HAp and SrHAp.

Parameter	Sample	
	HAp	SrHAp
Lattice parameter (Å)	$a = b = 9.471$	$a = b = 9.485$
	$c = 6.917$	$c = 6.951$
Cell volume, V (Å^3)	537.32	541.56
Microstrain, ε ($\times 10^{-3}$)	1.53	2.39
Crystallinity, CI (%)	91.1	64.6
Density, ρ (g/cm^3)	3.10	3.12

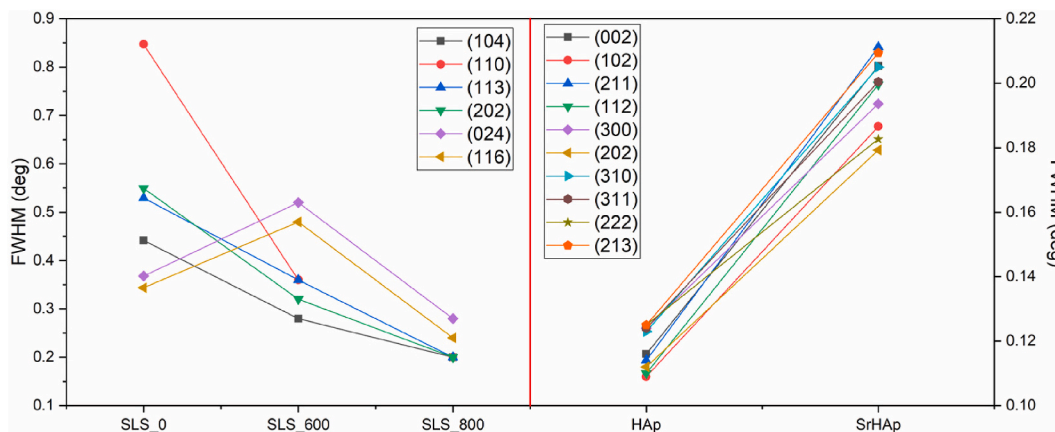**Fig. 4.** FWHM measured for various peaks of the samples.

Where β_m is the measured broadening, β_i is the instrumental broadening, and β_d is the corrected broadening. In this study, a silicon-based material used as a standard material for calibrating instrumental errors. The corrected physical broadening is defined as full width at half maximum (FWHM). Therefore, crystallite size can be calculated using the Scherrer equation, as described in Equation (9).

$$D = \frac{K\lambda}{\beta_d \cdot cos\,\theta} \tag{9}$$

Where K is the shape factor (0.89), λ is the wavelength of the X-ray radiation (Cu K α_1 = 1.5406 Å), and D is the crystallite size. The crystallite size values according to each diffraction plane of the samples are presented in Table 3. The average crystallite sizes are as follows: SLS_0 = 20.33 nm, SLS_600 = 23.87 nm, SLS_800 = 42.61 nm, SLS_1000 = 15.36 nm, HAp = 70.93 nm, and SrHAp = 46.90

Table 3
Crystallite size of the samples using average Scherrer method.

Crystallite size (nm)					
SLS_0	SLS_600	SLS_800	SLS_1000	HAp	SrHAp
28.57	23.51	52.91	14.21	73.37	41.44
19.45	30.62	42.87	19.87	78.58	45.90
10.30	24.22	43.60	13.86	75.64	40.82
16.67	24.47	44.05	10.34	78.47	43.23
16.28	27.87	44.59	17.06	69.74	44.66
24.58	17.42	32.35	16.85	77.44	48.36
26.47	18.95	37.89		71.70	43.01
				71.63	44.30
				72.25	49.40
				72.63	43.33
				71.32	49.57
				71.05	52.53
				68.62	47.55
				63.20	55.01
				48.31	54.09
20.33	23.87	42.61	15.36	70.93	46.90

nm.

3.3. Linear straight-line Scherrer method

In the linear straight-line Scherrer method, Equation (9) is rearranged as shown in Equation (10). This rearrangement yields plots of $cos\,\theta$ vs $1/\beta_d$ for all synthesized samples as illustrated in Fig. 5. The crystallite size values can be extracted from the slope, which is
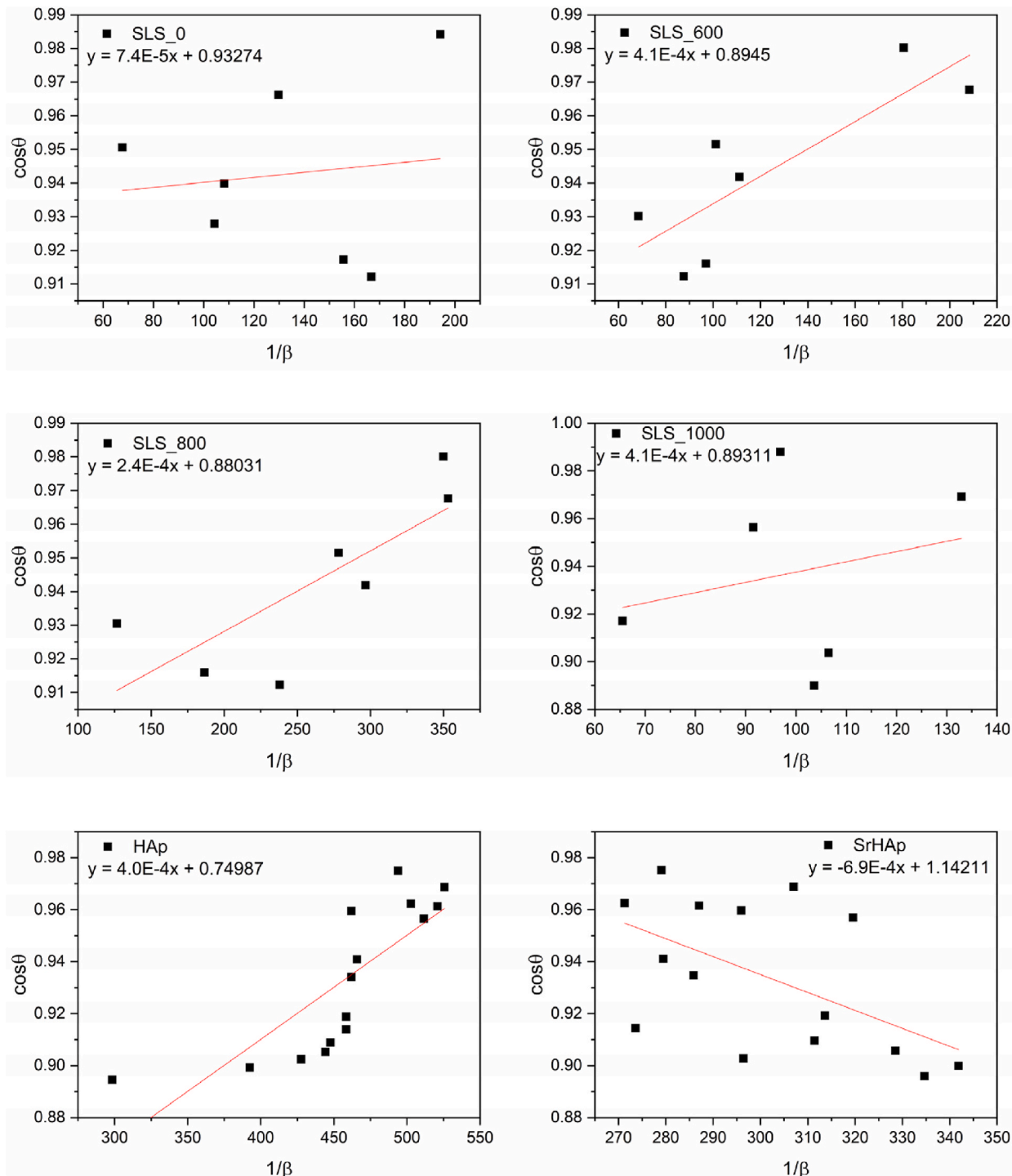

Fig. 5. Linear fit plot of linear straight-line Scherrer method of SLS_0, SLS_600, SLS_800, SLS_1000, HAp, and SrHAp.

equal to $K\lambda/D$, The calculated crystallite sizes were 1342.3, 232.1, 417.8, 245.5, 249.60, and 144.89 for SLS_0, SLS_600, SLS_800, SLS_1000, HAp, and SrHAp, respectively.

$$cos\,\theta = \frac{K\lambda}{D}\cdot\frac{1}{\beta_d} \tag{10}$$

These unusually large values deviated considerably from the typical crystallite sizes observed using XRD, which generally range
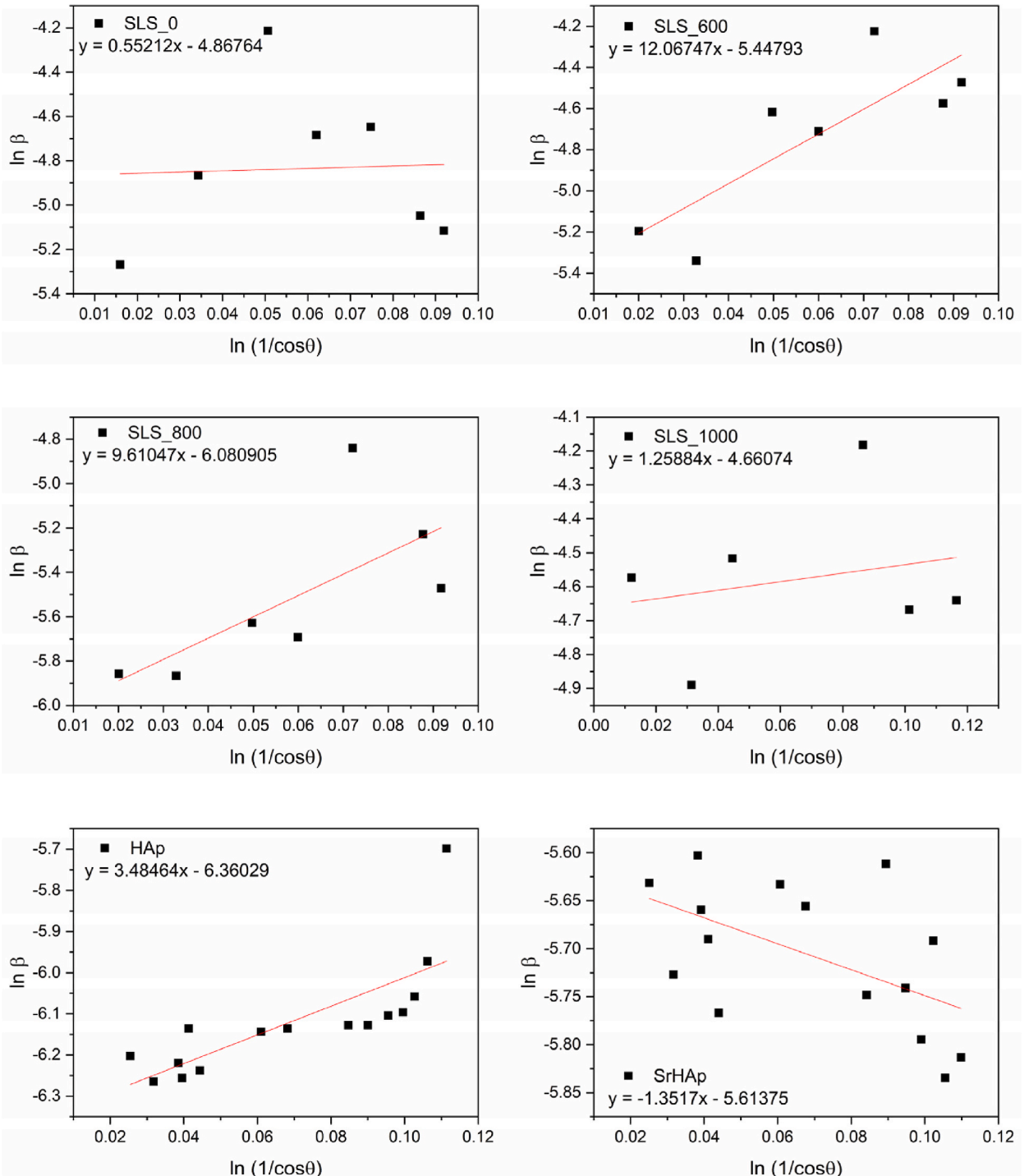

Fig. 6. Linear fit plot of Monshi-Scherrer method of SLS_0, SLS_600, SLS_800, SLS_1000, HAp, and SrHAp.

from 10 to 100 nm [31,43–46]. Therefore, this discrepancy suggests that the linear straight-line Scherrer method is not accurate for determining crystallite size, as indicated by previous studies [47,48]. The Scherrer equation presumes that peak broadening is solely due to finite crystallite size. When applying the linear straight-line Scherrer method, this assumption extends to a linear relationship between the variables. However, the relationship between $cos\,\theta$ and $1/\,\beta_d$ might not be perfectly linear due to complex broadening mechanisms [49].

3.4. Monshi-Scherrer method

The Monshi-Scherrer method, introduced by Monshi et al. (2012), modifies the original Scherrer equation to account for the influence of increasing crystallite size on XRD measurements [23]. This method corrects for changes in interplanar spacing (d_{hkl}) and $2\,\theta$ values, where $\beta\,cos\,\theta$ does not remain constant. This correction is important because it addresses the increasing values of crystallite size while the d_{hkl} values decrease and $2\,\theta$ values increase [23,47]. Furthermore, the Monshi-Scherrer method also provides an improvement to minimize error or $\sum(\pm\Delta ln\,\beta)^2$, leading to more accurate results for the diffraction peaks [23]. Therefore, the Monshi-Scherrer method is expressed in Equation (11).

$$\ln\beta = \ln\frac{1}{cos\,\theta} + \ln\frac{K\lambda}{D} \tag{11}$$

Graphs can be plotted with $\ln\beta$ vs $\ln\frac{1}{cos\,\theta}$ as illustrated in Fig. 6. From these linear plots, the crystallite size can be calculated using their intercept, as presented in Equation (12). The intercept values of SLS_0, SLS_600, SLS_800, SLS_1000, HAp, and SrHAp are -4.86764, −5.44793, −6.080905, −4.66074, −6.36029, −5.61375, respectively. The corresponding crystallite size values calculated from these intercepts are 18.83 nm, 33.64 nm, 63.35 nm, 15.31 nm, 83.76 nm, and 39.7 nm.

$$\frac{K\lambda}{D} = e^{(intercept)} \tag{12}$$

3.5. Williamson-Hall plot analysis

The Scherrer equation primarily considers XRD peak broadening due to the influence of crystallite size, neglecting the microstructures of the lattice, such as the intrinsic strain. Such strain can arise from point defects, grain boundaries, triple junctions, and stacking faults [50]. To overcome this limitation, methods like the Warren-Averbach method and the Williamson-Hall (W-H) method have been developed to incorporate the effects of microstrain on XRD peak broadening and to evaluate additional geometrical parameters of the crystal lattice. Among these methods, the W-H method is widely regarded as a precise, simple, and preferred technique [51,52]. The W-H method posits that the total peak broadening (Equation (13)) results from the combination of broadening due to crystallite size and strain-induced broadening.

$$\beta_{total} = \beta_{size} + \beta_{strain} \tag{13}$$

In addition to estimating crystallite size, the W-H method enables the assessment of other geometrical parameters, such as microstrain, stress, and energy density. It includes models such as the Uniform Deformation Model (UDM), Uniform Stress Deformation Model (USDM), and Uniform Deformation Energy Density Model (UDEDM), which will be discussed in detail below.

3.5.1. Uniform deformation model (UDM)

The UDM accounts for uniform intrinsic strain along the crystal directions, reflecting the isotropic nature of the crystal [53,54]. This uniform strain affects the broadening of diffraction peaks. The mathematical expression for this strain can be derived from Equation (13), providing the following relation.

$$\beta_{strain} = 4\varepsilon\,tan\,\theta \tag{14}$$

Since the W-H method considers that the broadening of a particular diffraction peak (β_{hkl}) is influenced by both intrinsic strain and the crystallite size, this relation is expressed in Equation (15) and Equation (16).

$$\beta_{hkl} = \beta_{size} + \beta_{strain} \tag{15}$$

$$\beta_{hkl} = \frac{K\lambda}{Dcos\theta} + 4\varepsilon\,tan\,\theta \tag{16}$$

Re-arranging Equation (16), we get,

$$\beta_{hkl}\cdot cos\,\theta = \frac{K\lambda}{D} + 4\varepsilon\,sin\,\theta \tag{17}$$

Equation (17) represents the UDM method with a consideration of the isotropic nature of the crystal, plotting $4\,sin\,\theta$ along the x-axis and $\beta_{hkl}\,cos\,\theta$ along the y-axis (Fig. 7). The slope (m) is used to determine the microstrain (m = ε), while the y-intercept is used to assess the crystallite size (D = $K\lambda$/y-intercept). The intercepts of the synthesized samples were found to be 0.00742, 0.00313, 0.00171, 0.00925, 0.00135, and 0.004 for SLS_0, SLS_600, SLS_800, SLS_1000, HAp, and SrHAp. From these intercepts, the crystallite sizes were

calculated as 19.52 nm, 46.27 nm, 85.19 nm, 15.66 nm, 107.27 nm, and 35.58 nm, respectively. The corresponding microstrain values were 0.0004, 0.00243, 0.0014, 0.00044, 0.00052, and 0.00068 for SLS_0, SLS_600, SLS_800, SLS_1000, HAp, and SrHAp, respectively.

3.5.2. Uniform stress deformation model (USDM)

While the UDM assumes uniform intrinsic strain in all directions within the crystal, the USDM provides an anisotropic approach, which is more reliable for a realistic crystal. The USDM relates to the influence of lattice deformation stress, assuming it is uniform along all lattice plane directions and is particularly useful for small microstrains [50,55]. The USDM applies principles from Hooke's
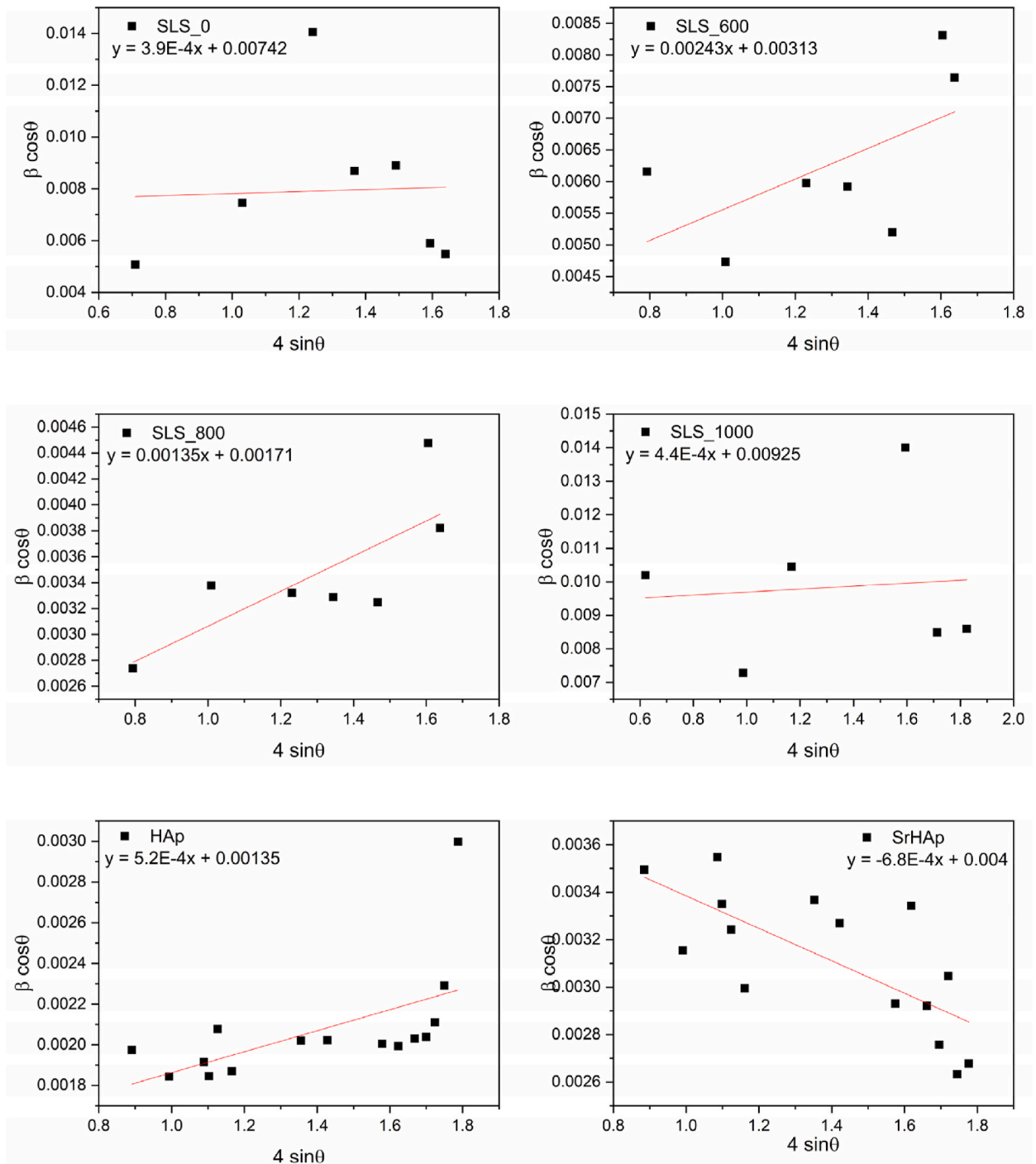

Fig. 7. Linear fit plot of UDM method of SLS_0, SLS_600, SLS_800, SLS_1000, HAp, and SrHAp.

law, which describes the linear relation between strain (ε) and stress (σ) as shown in Equation (18).

$$\sigma = Y\varepsilon \tag{18}$$

Where Y is Young's modulus. For this study, the values of Young's modulus were 77.6 GPa for calcite, 48.57 GPa for portlandite, and 6 GPa for hydroxyapatite. Rearranging and incorporating this into Equation (17), the modified equation becomes:
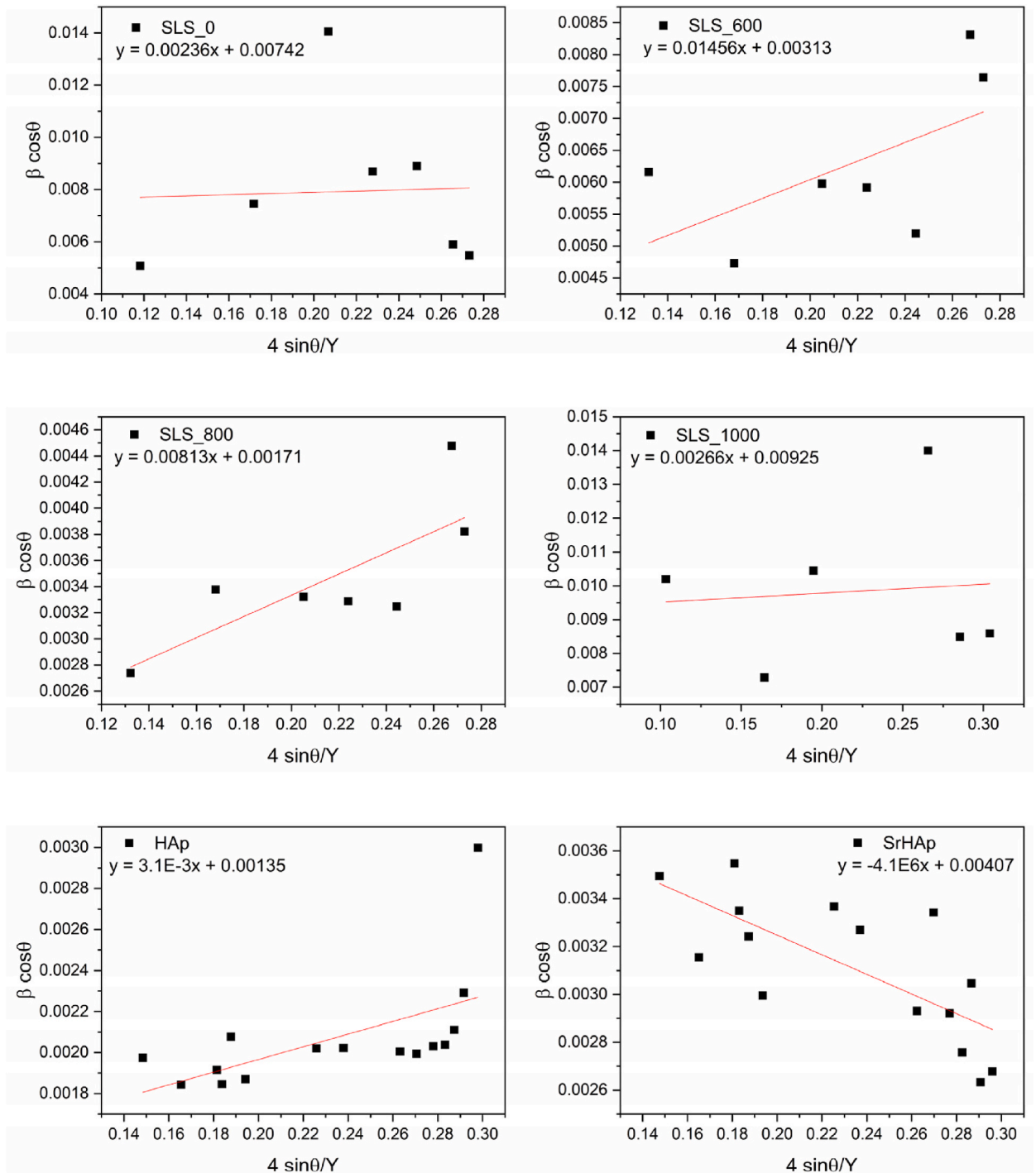

Fig. 8. Linear fit plot of USDM method of SLS_0, SLS_600, SLS_800, SLS_1000, HAp, and SrHAp.

$$\beta_{hkl} \cdot \cos\theta = \frac{K\lambda}{D \cdot \cos\theta} + 4\sigma\, \frac{\sin\theta}{Y_{hkl}} \qquad (19)$$

Plots according to Equation (19) were presented in Fig. 8 with $4\sin\theta/Y$ along the x-axis and $\beta_{hkl}\cos\theta$ along the y-axis. The slope of the graphs is equal to the value of stress, which is obtained as 30.71, 188.3, 105.1, 21.52, 3.1, and 4.1 MPa for SLS_0, SLS_600, SLS_800, SLS_1000, HAp, and SrHAp, respectively. Microstrain values can be obtained using equation (18), which gives the microstrain values of 0.00040, 0.00243, 0.00135, 0.00044, 0.00052, and 0.00068. The crystallite sizes obtained from this model were 19.52 nm, 46.27 nm, 84.69 nm, 15.66 nm, 107.27 nm, and 35.58 nm for SLS_0, SLS_600, SLS_800, SLS_1000, HAp, and SrHAp, respectively.
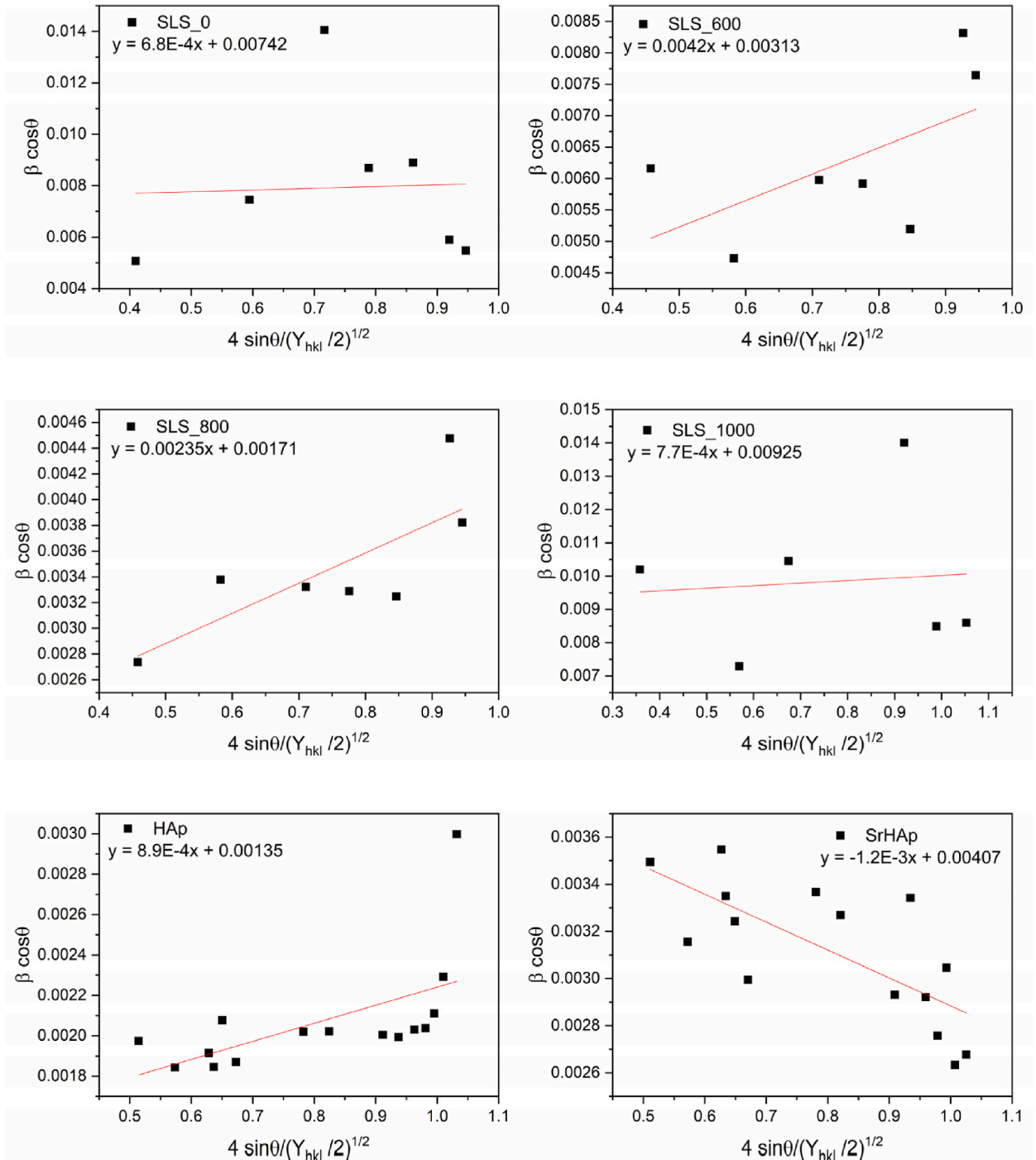

Fig. 9. Linear fit plot of UDEDM method of SLS_0, SLS_600, SLS_800, SLS_1000, HAp, and SrHAp.

3.5.3. Uniform deformation energy density model (UDEDM)

The UDM only can work in considering a perfectly isotropic crystal. However, in mostly real crystals, the imperfections between lattices occur for a particular reason. Prior to this, the USDM regards the intrinsic strain in the crystal as anisotropic according to Hooke's law. The difference between the USDM and the UDEDM is that the UDEDM can measure the anisotropic energy, which is essential for real crystals that produce crystallographic imperfections that may prevent Hook's law linear relation between stress and strain. Therefore, the UDEDM came up with an idea to consider the stress-strain relation as a function of energy density (u), as described by Equation (20) [53].
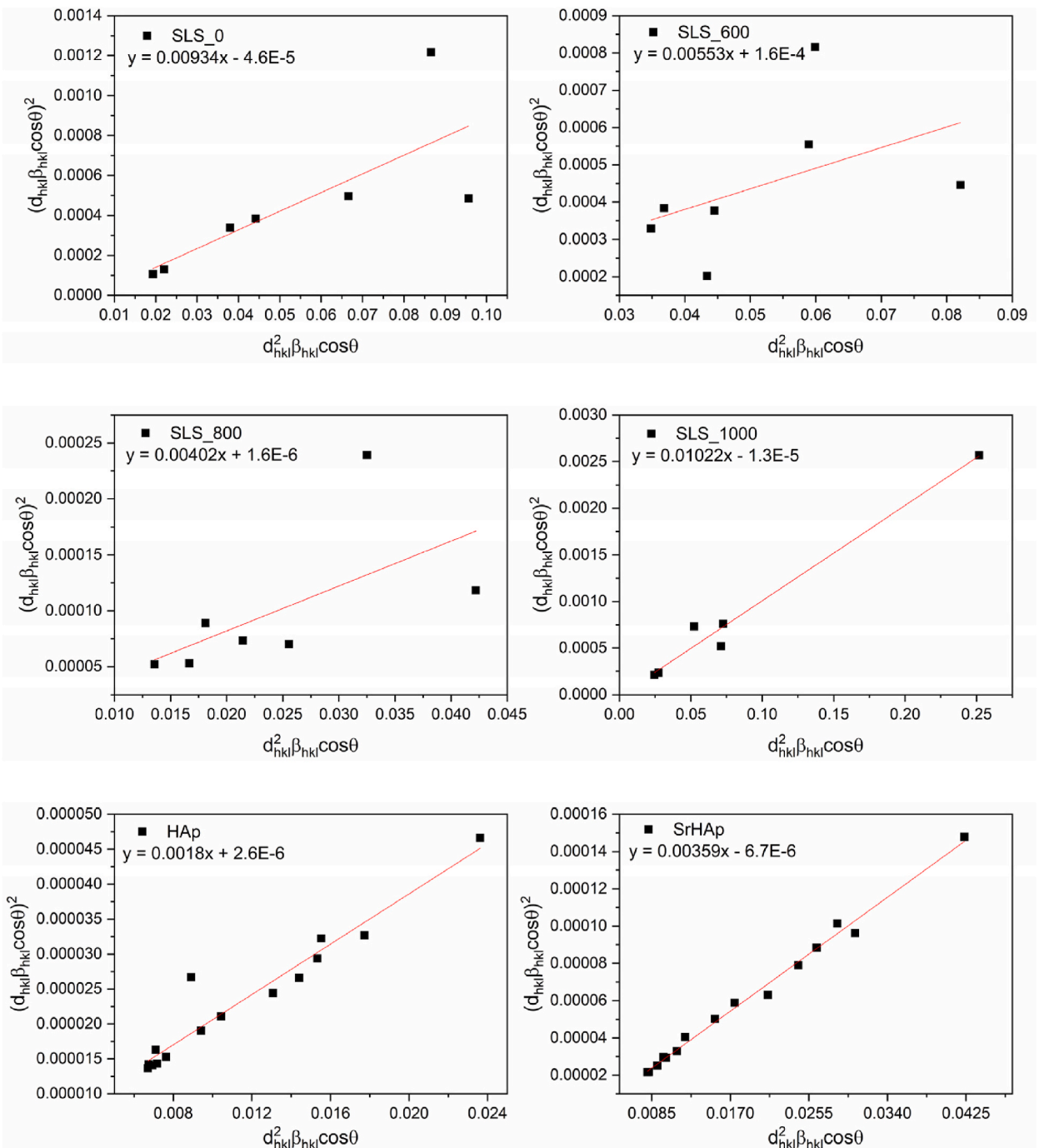

Fig. 10. Linear fit plot of SSP method of SLS_0, SLS_600, SLS_800, SLS_1000, HAp, and SrHAp.

$$u = \frac{Y_{hkl}}{2} \cdot \varepsilon^2 \tag{20}$$

Rearranging Equation (20), we get

$$\varepsilon = \sigma \cdot \sqrt{\frac{2u}{Y_{hkl}}} \tag{21}$$

Substituting this into Equation (17), the UDEDM is expressed as:

$$\beta_{hkl} \cdot \cos\theta = \frac{K\lambda}{D \cdot \cos\theta} + 4 \sin\theta \cdot \sqrt{\frac{2u}{Y_{hkl}}} \tag{22}$$

Equation (22) describes the UDEDM with the stress-strain relation based on energy density. Graphs of the plot of $4 \sin\theta/(Y/2)^{1/2}$ along the x-axis and $\beta_{hkl} \cos\theta$ along the y-axis display in Fig. 9. The crystallite size values were 19.52 nm, 46.27 nm, 84.69 nm, 15.66 nm, 107.27 nm, and 35.58 nm for SLS_0, SLS_600, SLS_800, SLS_1000, HAp, and SrHAp, respectively. The slope provided the energy density as 6.10, 228.01, 70.56, 4.75, 0.80, and 1.40 (kJ/m^3) for SLS_0, SLS_600, SLS_800, SLS_1000, HAp, and SrHAp. Microstrain values derived from Equation (20) were 0.00040, 0.00242, 0.00134, 0.00044, 0.00052, and 0.00069 for SLS_0, SLS_600, SLS_800, SLS_1000, HAp, and SrHAp, respectively.

3.6. Size-strain plot (SSP) analysis

The Williamson-Hall method evaluates peak broadening as a function of the diffraction angle (2θ). In contrast, the SSP method provides a different approach by considering the XRD peak profile as a combination of Lorentzian and Gaussian functions. The strain profile follows a Gaussian function, whereas the crystallite size profile is described by a Lorentzian function, which is expressed by Equation (23). Moreover, the SSP method consistently yields superior results for isotropic broadening, as it prioritizes low-angle reflections, which offer greater accuracy and precision compared to high-angle reflections. This is due to the fact that XRD data at higher angles are of lower quality, and peaks tend to overlap significantly at higher diffraction angle [18,56].

$$\beta_{hkl} = \beta_L + \beta_G \tag{23}$$

Where β_L and β_G are the peak broadening according to Lorentzian and Gaussian functions. Here is the equation for the SSP method [53,57,58]

$$(d_{hkl} \cdot \beta_{hkl} \cdot \cos\theta)^2 = \frac{K\lambda}{D} \cdot \left(d_{hkl}^2 \cdot \beta_{hkl} \cdot \cos\theta\right) + \left(\frac{\varepsilon}{2}\right)^2 \tag{24}$$

The SSP plots for the prepared samples are shown in Fig. 10. The term $d_{hkl}^2 \cdot \beta_{hkl} \cdot \cos\theta$ is plotted along the x-axis with respect to $(d_{hkl} \cdot \beta_{hkl} \cdot \cos\theta)^2$ along the y-axis. The slope and the y-intercept of the plots give information about crystallite size and microstrain values. The crystallite size values of SLS_0, SLS_600, SLS_800, SLS_1000, HAp, and SrHAp were 15.5, 26.19, 36.02, 14.17, 80.45, and 40.23 nm. The microstrain values can only be calculated for SLS_600, SLS_800, and HAp because they had a positive y-intercept. Therefore, the microstrain values were calculated as 0.00630, 0.00063, and 0.00087 for SLS_600, SLS_800, and HAp, respectively.

3.7. Halder-Wagner (HW) method analysis

As opposed to the SSP method which considers a combination of Lorentzian and Gaussian functions for the peak profile broadening, the HW method assumes that the peak broadening is a symmetric Voigt function [59,60]. This method has the advantage of giving more weight to peaks in the low and mid-angle range, where diffracting peak overlap is minimal [28,50]. The HW method involves the convolution of Lorentzian and Gaussian functions [61], which gives the expression below.

$$\beta_{hkl}^2 = \beta_L \cdot \beta_{hkl} + \beta_G^2 \tag{25}$$

Where β_L and β_G are the full width at half maximum of the Lorentzian and Gaussian functions, respectively. The HW method gives the relation of crystallite size and microstrains as follows.

$$\left(\frac{\beta_{hkl}^*}{d_{hkl}^*}\right)^2 = \frac{1}{D} \cdot \frac{\beta_{hkl}^*}{d_{hkl}^{*\,2}} + \left(\frac{\varepsilon}{2}\right)^2 \tag{26}$$

$$\beta_{hkl}^* = \beta_{hkl} \cdot \frac{\cos\theta}{\lambda} \tag{27}$$

$$d_{hkl}^* = 2d_{hkl} \cdot \frac{\sin\theta}{\lambda} \tag{28}$$

Using Equation (26), plots of the HW method are presented in Fig. 11. A plot of $\frac{\beta_{hkl}^*}{d_{hkl}^{*\,2}}$ on the x-axis and $\left(\frac{\beta_{hkl}^*}{d_{hkl}^*}\right)^2$ on the y-axis gives a

slope of $1/D$ and a y-intercept of $\left(\frac{\varepsilon}{2}\right)^2$. This provided information on crystallite size and microstrain, respectively. After calculation, the crystallite size of SLS_0, SLS_600, SLS_800, SLS_1000, HAp, and SrHAp are 16.50, 27.86, 38.31, 15.06, 32.26, and 25 nm, respectively. Since the y-intercept is equal to $\left(\frac{\varepsilon}{2}\right)^2$, the negative y-intercept cannot be calculated for microstrain values. Therefore, microstrain could only be calculated for SLS_600 and SLS_800. The microstrain values of SLS_600 and SLS_800 were 0.00409 and 0.00041, respectively.
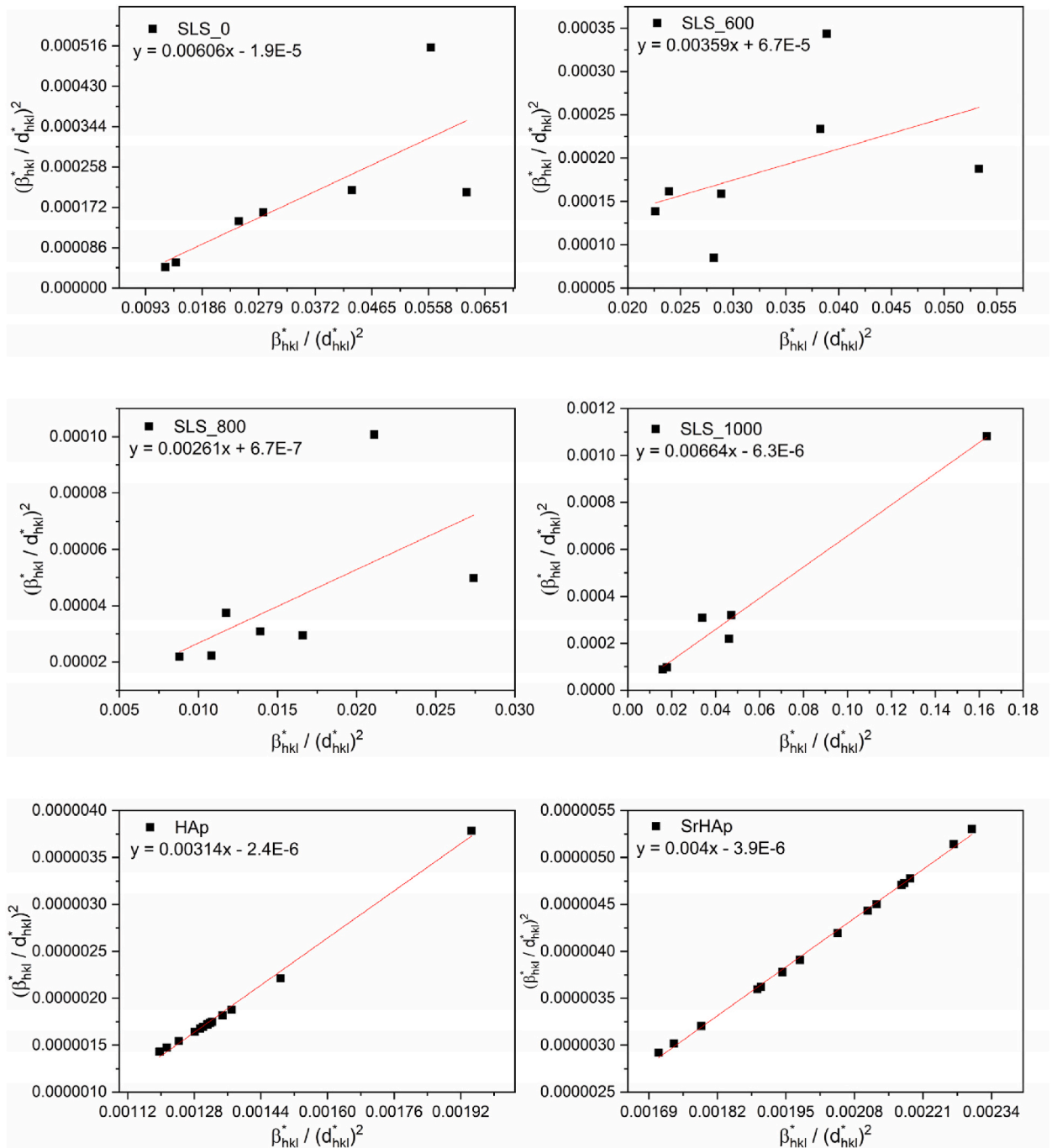

Fig. 11. Linear fit plot of HW method of SLS_0, SLS_600, SLS_800, SLS_1000, HAp, and SrHAp.

3.8. TEM analysis

TEM investigation provides insight into the particle size (S) and shape of HAp and SrHAp. The TEM morphology images of the HAp and SrHAp are displayed in Fig. 12. The images revealed that both HAp and SrHAp exhibited agglomerated particles with HAp showing a nearly spherical shape and SrHAp presenting a rod-like shape. The morphology of SrHAp was notably more elongated, similar to findings reported by Frasnelli et al. [62]. The particle size of HAp was estimated to be around 110–120 nm, while the particle size of SrHAp was measured to be around 63×130 nm. This increasing particle size of SrHAp also reported by previous studies [40,63].

Table 4 summarizes the results obtained from the Scherrer method, linear straight-line Scherrer method, Monshi-Scherrer method, W-H plots, SSP method, HW method and TEM. The values of crystallite size obtained from the linear straight-line Scherrer method showed excessive deviation, indicating its inaccuracy and impracticality for values above 100 nm, as also reported in previous research. Previous research also reported that inaccuracy [47,52,64]. In exceptional cases for HAp and SrHAp, the linear straight-line Scherrer method produced much lower crystallite sizes. The Monshi-Scherrer method produced more reliable results indicating its inaccuracy and impracticality for values above 100 nm, as also reported in previous research. Apart from the Scherrer-related method, the W-H method accounts for peak broadening due to lattice strain, not solely depending on the crystallite size. This strain (micro-strain) forms in the structure due to various defects such as point defects, grain boundaries, stacking faults, and others [50,65]. The W-H method offers a comprehensive analysis of geometrical properties, including stress, microstrain, and energy density. The W-H method consistently provided reliable values for crystallite size and microstrain across all samples, consistent with previous studies [48,52,64,66,67]. Negative slopes in the W-H plots interpret a compression strain in the samples, while others believe that these negative slopes may not have a significant impact [28,68]. The SSP and HW methods are quite identical for the peak broadening, which takes account into the peak profiles of Lorentzian and Gaussian. For isotropic crystals, these methods perform better by giving more weight to lower-angle peaks and less to higher-angle peaks in the XRD pattern [50,69,70]. Thus, the crystallite size results of the SSP and HW methods showed slight deviations for SLS samples. However, to calculate the microstrain, the SSP and HW methods require positive y-intercepts. For further investigation, TEM analysis was employed to determine the particle size and shape of HAp and SrHAp. The particle size results align well with the crystallite size obtained from most methods, except for the linear straight-line Scherrer method. This is because the calculated crystallite size did not exceed the particle size. In other words, the crystallite size must be less than the particle size of nanoparticles.

According to Table 4 (except the linear straight-line Scherrer method), the crystallite size of SLS samples increased with calcination temperature for SLS_0, SLS_600, and SLS_800, regardless of the method used. This trend is consistent with previous studies [71,72]. The increase in crystallite size with calcination temperature is attributed to enhanced crystal growth, improved structural uniformity, and reduced defects [73]. The decrease in microstrain was evidenced from SLS_600 to SLS_800 using the W-H plots, SSP method, and HW method. SLS_1000 was excluded because it had already possessed a different crystal structure from the others. The SLS_1000 showed the most constant value of crystallite size(~15 nm), indicating its suitability for all methods used. Furthermore, the crystallite size of SrHAp was consistently smaller than that of HAp across all methods. This reduction can be attributed to the Sr^{2+} substitution, which distorts the hexagonal lattice structure of HAp [14,15,41]. According to the W-H method, this distortion results in increased microstrain in SrHAp compared to HAp.

4. Conclusion

HAp and SrHAp were successfully synthesized using the hydrothermal method with sand lobster shell waste. XRD analysis indicated that a calcination temperature of 1000 $^\circ$ C for the SLS was suitable for the preparation of HAp and SrHAp. The SLS_1000 exhibited a $Ca(OH)_2$ phase (portlandite), while the other SLS retained a $CaCO_3$ phase (calcite). The HAp and SrHAp exhibited diffraction patterns according to the reference. The crystallinity of SrHAp decreased due to the distortion of crystal lattice caused by the Sr^{2+} substitution, which has a longer ionic radius than Ca^{2+}. Crystallite size and other geometrical parameters were analyzed using the Scherrer method, linear straight-line Scherrer method, Monshi-Scherrer method, W-H plots, SSP method, HW method, and TEM. Except for the linear straight-line Scherrer method, all methods were suitable for analyzing the XRD data of SLS, HAp, and SrHAp. Each method provides a variety of different approaches. The Monshi-Scherrer method offered improved results over the linear straight-line Scherrer method, providing values of crystallite size that were closer to those obtained using the standard Scherrer method. The W-H plots introduced considerations of anisotropic elasticity, which provides additional information on microstrain, stress, and energy density. This method provided the most consistent values for crystallite size. The SSP and HW methods, while also yielding reasonable crystallite size values with minor deviations, were limited in their ability to determine microstrain accurately, particularly when y-intercepts were negative. TEM results confirmed that, with the exception of the linear straight-line Scherrer method, all methods were effective for estimating crystallite size. Overall, the W-H method proved to be the most reliable for determining crystal properties due to its comprehensive analysis of strain and stress, along with consistent crystallite size measurements.

CRediT authorship contribution statement

Arian Hermawan Diputra: Writing – original draft, Visualization, Methodology, Investigation, Formal analysis, Conceptualization. **I Kadek Hariscandra Dinatha:** Writing – review & editing, Validation, Supervision, Data curation, Conceptualization. **Yusril Yusuf:** Validation, Supervision, Resources, Project administration, Funding acquisition, Conceptualization.
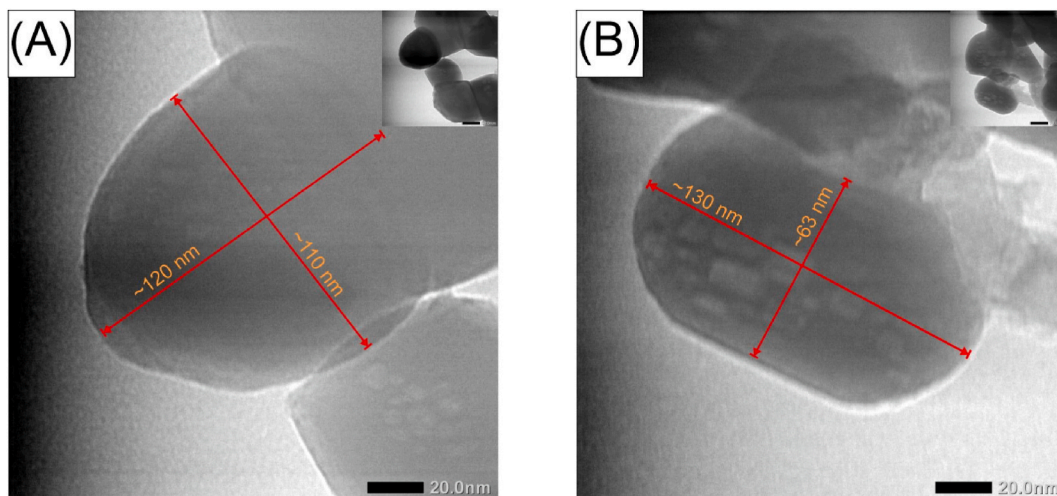
Fig. 12. TEM images of (a) HAp and (b) SrHAp.

Table 4
Crystallite size, particle size, and other geometrical parameters of SLS, HAp, and SrHAp.

Methods		Sample					
		SLS_0	SLS_600	SLS_800	SLS_1000	HAp	SrHAp
Average Scherrer	D (nm)	20.33	23.87	42.61	15.36	70.93	46.88
Linear straight-line Scherrer	D (nm)	1342.34	232.07	417.80	245.48	32.26	25.00
Monshi-Scherrer	D (nm)	18.83	33.64	63.35	15.31	83.76	39.70
W-H UDM	D (nm)	19.52	46.27	85.19	15.66	107.27	35.58
	$\varepsilon\ (\times 10^{-3})$	0.40	2.43	1.40	0.44	0.52	0.68
W-H USDM	D (nm)	19.52	46.27	84.69	15.66	107.27	35.58
	$\varepsilon\ (\times 10^{-3})$	0.40	2.43	1.36	0.44	0.52	0.68
	σ (MPa)	30.71	188.3	105.1	21.52	3.10	4.10
W-H UDEDM	D (nm)	19.52	46.27	84.69	15.66	107.27	35.58
	$\varepsilon\ (\times 10^{-3})$	0.40	2.42	1.34	0.44	0.52	0.69
	u (kJ/m^3)	0.47	17.64	5.52	0.59	0.80	1.40
SSP	D (nm)	15.50	26.19	36.02	14.17	80.45	40.23
	$\varepsilon\ (\times 10^{-3})$	–	6.30	0.63	–	0.87	–
Halder-Wagner	D (nm)	16.50	27.86	38.31	15.06	32.26	25.00
	$\varepsilon\ (\times 10^{-3})$	–	4.09	0.41	–	–	–
TEM	S (nm)	–	–	–	–	~110	63 × 130

Declaration of competing interest

The authors declare that they have no known competing financial interests or personal relationships that could have appeared to influence the work reported in this paper.

Appendix A. Supplementary data

Supplementary data to this article can be found online at https://doi.org/10.1016/j.heliyon.2025.e41781.

References

[1] H. Shi, Z. Zhou, W. Li, Y. Fan, Z. Li, J. Wei, Hydroxyapatite based materials for bone tissue engineering: a brief and comprehensive introduction, Crystals 11 (2021) 149, https://doi.org/10.3390/cryst11020149.

[2] D.J. Patty, A.D. Nugraheni, I.D. Ana, Y. Yusuf, In vitro bioactivity of <scp>3D</scp> microstructure hydroxyapatite/collagen based-egg white as an antibacterial agent, J. Biomed. Mater. Res. B Appl. Biomater. 110 (2022) 1412–1424, https://doi.org/10.1002/jbm.b.35009.

[3] D.J. Patty, A.D. Nugraheni, I.D. Ana, Aminatun, Y.W. Sari, Gunawarman, Y. Yusuf, The enhanced properties and bioactivity of poly-ε-caprolactone/poly lactic-co-glycolic acid doped with carbonate hydroxyapatite–egg white, RSC Adv. 13 (2023) 34427–34438, https://doi.org/10.1039/D3RA07486B.

[4] M. Sari, P. Hening, Chotimah, I.D. Ana, Y. Yusuf, Porous structure of bioceramics carbonated hydroxyapatite-based honeycomb scaffold for bone tissue engineering, Mater. Today Commun. 26 (2021) 102135, https://doi.org/10.1016/j.mtcomm.2021.102135.

[5] U. Anjaneyulu, B. Priyadarshini, A. Nirmala Grace, U. Vijayalakshmi, Fabrication and characterization of Ag doped hydroxyapatite-polyvinyl alcohol composite nanofibers and its in vitro biological evaluations for bone tissue engineering applications, J. Sol. Gel Sci. Technol. 81 (2017) 750–761, https://doi.org/10.1007/s10971-016-4243-5.

[6] M. Sari, P. Hening, Chotimah, I.D. Ana, Y. Yusuf, Bioceramic hydroxyapatite-based scaffold with a porous structure using honeycomb as a natural polymeric Porogen for bone tissue engineering, Biomater. Res. 25 (2021), https://doi.org/10.1186/s40824-021-00203-z.

[7] S. Hussain, K. Sabiruddin, Effect of heat treatment on the synthesis of hydroxyapatite from Indian clam seashell by hydrothermal method, Ceram. Int. 47 (2021) 29660–29669, https://doi.org/10.1016/j.ceramint.2021.07.137.

[8] M. Sari, A. Ashilawati, L. Khoir, R. Wahyuningsih, Y. Yusuf, Carbonated hydroxyapatite extracted from Indonesian's eggshell biogenic wastes as bioceramic materials, Journal of Biomimetics, Biomaterials and Biomedical Engineering 62 (2023) 1–7, https://doi.org/10.4028/p-xp22Cc.

[9] I. Pawarangan, Y. Yusuf, Characteristics of hydroxyapatite from buffalo bone waste synthesized by precipitation method, in: IOP Conf Ser Mater Sci Eng, Institute of Physics Publishing, 2018, https://doi.org/10.1088/1757-899X/432/1/012044.

[10] E. Barua, A. Das, D. Pamu, A.B. Deoghare, P. Deb, S. Das Lala, S. Chatterjee, Effect of thermal treatment on the physico-chemical properties of bioactive hydroxyapatite derived from caprine bone bio-waste, Ceram. Int. 45 (2019) 23265–23277, https://doi.org/10.1016/j.ceramint.2019.08.023.

[11] M.A. Jamilludin, I.K.H. Dinatha, A.I. Supii, J. Partini, D.L. Kusindarta, Y. Yusuf, Functionalized cellulose nanofibrils in carbonate-substituted hydroxyapatite nanorod-based scaffold from long-spined sea urchin (Diadema setosum) shells reinforced with polyvinyl alcohol for alveolar bone tissue engineering, RSC Adv. 13 (2023) 32444–32456, https://doi.org/10.1039/D3RA06165E.

[12] C.E. Davies, M.M.A. Whitten, A. Kim, E.C. Wootton, T.G.G. Maffeis, M. Tlusty, C.L. Vogan, A.F. Rowley, A comparison of the structure of American (Homarus americanus) and European (Homarus gammarus) lobster cuticle with particular reference to shell disease susceptibility, J. Invertebr. Pathol. 117 (2014) 33–41, https://doi.org/10.1016/j.jip.2014.01.001.

[13] V. Lalzawmliana, A. Anand, P. Mukherjee, S. Chaudhuri, B. Kundu, S.K. Nandi, N.L. Thakur, Marine organisms as a source of natural matrix for bone tissue engineering, Ceram. Int. 45 (2019) 1469–1481, https://doi.org/10.1016/j.ceramint.2018.10.108.

[14] A. Ressler, A. Žužić, I. Ivanišević, N. Kamboj, H. Ivanković, Ionic substituted hydroxyapatite for bone regeneration applications: a review, Open Ceramics 6 (2021) 100122, https://doi.org/10.1016/j.oceram.2021.100122.

[15] L. Stipniece, S. Wilson, J.M. Curran, R. Chen, K. Salma-Ancane, P.K. Sharma, B.J. Meenan, A.R. Boyd, Strontium substituted hydroxyapatite promotes direct primary human osteoblast maturation, Ceram. Int. 47 (2021) 3368–3379, https://doi.org/10.1016/j.ceramint.2020.09.182.

[16] G. Hulsart-Billström, W. Xia, E. Pankotai, M. Weszl, E. Carlsson, C. Forster-Horváth, S. Larsson, H. Engqvist, Z. Lacza, Osteogenic potential of Sr-doped calcium phosphate hollow spheres in vitro and in vivo, J. Biomed. Mater. Res. 101A (2013) 2322–2331, https://doi.org/10.1002/jbm.a.34526.

[17] M. Baier, P. Staudt, R. Klein, U. Sommer, R. Wenz, I. Grafe, P.J. Meeder, P.P. Nawroth, C. Kasperk, Strontium enhances osseointegration of calcium phosphate cement: a histomorphometric pilot study in ovariectomized rats, J. Orthop. Surg. Res. 8 (2013) 16, https://doi.org/10.1186/1749-799X-8-16.

[18] A. Khorsand Zak, W.H. Abd Majid, M.E. Abrishami, R. Yousefi, X-ray analysis of ZnO nanoparticles by Williamson–Hall and size–strain plot methods, Solid State Sci. 13 (2011) 251–256, https://doi.org/10.1016/j.solidstatesciences.2010.11.024.

[19] R. Das, S. Sarkar, X-ray diffraction analysis of synthesized silver nanohexagon for the study of their mechanical properties, Mater. Chem. Phys. 167 (2015) 97–102, https://doi.org/10.1016/j.matchemphys.2015.10.015.

[20] B. Sun, G. Haunschild, C. Polanco, J. Ju, L. Lindsay, G. Koblmüller, Y.K. Koh, Dislocation-induced thermal transport anisotropy in single-crystal group-III nitride films, Nat. Mater. 18 (2019) 136–140, https://doi.org/10.1038/s41563-018-0250-y.

[21] I. Madhi, W. Meddeb, B. Bouzid, M. Saadoun, B. Bessaïs, Effect of temperature and NO2 surface adsorption on electrical properties of screen printed ITO thin film, Appl. Surf. Sci. 355 (2015) 242–249, https://doi.org/10.1016/j.apsusc.2015.07.135.

[22] P. Bindu, S. Thomas, Estimation of lattice strain in ZnO nanoparticles: X-ray peak profile analysis, Journal of Theoretical and Applied Physics 8 (2014) 123–134, https://doi.org/10.1007/s40094-014-0141-9.

[23] A. Monshi, M.R. Foroughi, M.R. Monshi, Modified scherrer equation to estimate more accurately nano-crystallite size using XRD, World J. Nano Sci. Eng. 2 (2012) 154–160, https://doi.org/10.4236/wjnse.2012.23020.

[24] S. Das Bakshi, D. Sinha, S. Ghosh Chowdhury, Anisotropic broadening of XRD peaks of α′-Fe: Williamson-Hall and Warren-Averbach analysis using full width at half maximum (FWHM) and integral breadth (IB), Mater Charact 142 (2018) 144–153, https://doi.org/10.1016/j.matchar.2018.05.018.

[25] S. Brandstetter, P.M. Derlet, S. Van Petegem, H. Van Swygenhoven, Williamson–Hall anisotropy in nanocrystalline metals: X-ray diffraction experiments and atomistic simulations, Acta Mater. 56 (2008) 165–176, https://doi.org/10.1016/j.actamat.2007.09.007.

[26] Y.T. Prabhu, K.V. Rao, V.S.S. Kumar, B.S. Kumari, X-Ray Analysis by Williamson-Hall and size-strain plot methods of ZnO nanoparticles with fuel variation, World J. Nano Sci. Eng. 4 (2014) 21–28, https://doi.org/10.4236/wjnse.2014.41004.

[27] M.A. Tagliente, M. Massaro, Strain-driven (002) preferred orientation of ZnO nanoparticles in ion-implanted silica, Nucl. Instrum. Methods Phys. Res. B 266 (2008) 1055–1061, https://doi.org/10.1016/j.nimb.2008.02.036.

[28] S.A. Hassanzadeh-Tabrizi, Precise calculation of crystallite size of nanomaterials: a review, J. Alloys Compd. 968 (2023) 171914, https://doi.org/10.1016/j.jallcom.2023.171914.

[29] S.K. Sen, U.C. Barman, M.S. Manir, P. Mondal, S. Dutta, M. Paul, M.A.M. Chowdhury, M.A. Hakim, X-ray peak profile analysis of pure and Dy-doped α-MoO3 nanobelts using Debye-Scherrer, Williamson-Hall and Halder-Wagner methods, Adv. Nat. Sci. Nanosci. Nanotechnol. 11 (2020) 025004, https://doi.org/10.1088/2043-6254/ab8732.

[30] I.K.H. Dinatha, A.H. Diputra, H. Wihadmadyatami, J. Partini, Y. Yusuf, Nanofibrous electrospun scaffold doped with hydroxyapatite derived from sand lobster shell (Panulirus homarus) for bone tissue engineering, RSC Adv. 14 (2024) 8222–8239, https://doi.org/10.1039/D4RA00619D.

[31] I. Kadek Hariscandra Dinatha, M.A. Jamilludin, A.I. Supii, H. Wihadmadyatami, J. Partini, Y. Yusuf, Porous scaffold hydroxyapatite from sand lobster shells (<scp> Panulirus homarus </scp>) using polyethylene oxide/chitosan as polymeric porogen for bone tissue engineering, J. Biomed. Mater. Res. B Appl. Biomater. (2023), https://doi.org/10.1002/jbm.b.35341.

[32] Y. Sa, Y. Guo, X. Feng, M. Wang, P. Li, Y. Gao, X. Yang, T. Jiang, Are different crystallinity-index-calculating methods of hydroxyapatite efficient and consistent? New J. Chem. 41 (2017) 5723–5731, https://doi.org/10.1039/C7NJ00803A.

[33] N. Ishizawa, H. Setoguchi, K. Yanagisawa, Structural evolution of calcite at high temperatures: phase V unveiled, Sci. Rep. 3 (2013) 2832, https://doi.org/10.1038/srep02832.

[34] L. Desgranges, D. Grebille, G. Calvarin, G. Chevrier, N. Floquet, J.-C. Niepce, Hydrogen thermal motion in calcium hydroxide: Ca(OH)2, Acta Crystallogr. B 49 (1993) 812–817, https://doi.org/10.1107/S0108768193003556.

[35] A. Lesbani, P. Tamba, R. Mohadi, F. Fahmariyanti, Preparation of calcium oxide from Achatina fulica; as catalyst for production of biodiesel from waste cooking oil, Indonesian Journal of Chemistry 13 (2013) 176–180, https://doi.org/10.22146/ijc.21302.

[36] E. Serris, L. Favergeon, M. Pijolat, M. Soustelle, P. Nortier, R.S. Gärtner, T. Chopin, Z. Habib, Study of the hydration of CaO powder by gas–solid reaction, Cem Concr Res 41 (2011) 1078–1084, https://doi.org/10.1016/j.cemconres.2011.06.014.

[37] M.E. Fleet, X. Liu, Y. Pan, Site preference of rare earth elements in hydroxyapatite [Ca10(PO4)6(OH)2], J. Solid State Chem. 149 (2000) 391–398, https://doi.org/10.1006/jssc.1999.8563.

[38] P. Oberbek, T. Bolek, A. Chlanda, S. Hirano, S. Kusnieruk, J. Rogowska-Tylman, G. Nechyporenko, V. Zinchenko, W. Swieszkowski, T. Puzyn, Characterization and influence of hydroxyapatite nanopowders on living cells, Beilstein J. Nanotechnol. 9 (2018) 3079–3094, https://doi.org/10.3762/bjnano.9.286.

[39] Y. Wu, S. Bose, Nanocrystalline hydroxyapatite: micelle templated synthesis and characterization, Langmuir 21 (2005) 3232–3234, https://doi.org/10.1021/la046754z.

[40] Z.Y. Li, W.M. Lam, C. Yang, B. Xu, G.X. Ni, S.A. Abbah, K.M.C. Cheung, K.D.K. Luk, W.W. Lu, Chemical composition, crystal size and lattice structural changes after incorporation of strontium into biomimetic apatite, Biomaterials 28 (2007) 1452–1460, https://doi.org/10.1016/j.biomaterials.2006.11.001.

[41] J. Terra, E.R. Dourado, J.-G. Eon, D.E. Ellis, G. Gonzalez, A.M. Rossi, The structure of strontium-doped hydroxyapatite: an experimental and theoretical study, Phys. Chem. Chem. Phys. 11 (2009) 568–577, https://doi.org/10.1039/B802841A.

[42] M.D. O'Donnell, Y. Fredholm, A. de Rouffignac, R.G. Hill, Structural analysis of a series of strontium-substituted apatites, Acta Biomater. 4 (2008) 1455–1464, https://doi.org/10.1016/j.actbio.2008.04.018.

[43] I.K.H. Dinatha, M.A. Jamilludin, A.I. Supii, H. Wihadmadyatami, J. Partini, Y. Yusuf, Characteristics of bioceramic hydroxyapatite based on sand lobster shells (*Panulirus homarus*) as sources of calcium with optimal calcination temperature, Mater. Sci. Forum 1090 (2023) 39–44, https://doi.org/10.4028/p-c1qrat.

[44] V.J. Mawuntu, Y. Yusuf, Porous structure engineering of bioceramic hydroxyapatite-based scaffolds using PVA, PVP, and PEO as polymeric porogens, Journal of Asian Ceramic Societies 7 (2019) 161–169, https://doi.org/10.1080/21870764.2019.1595927.

[45] A. Bigi, E. Boanini, C. Capuccini, M. Gazzano, Strontium-substituted hydroxyapatite nanocrystals, Inorganica Chim Acta 360 (2007) 1009–1016, https://doi.org/10.1016/j.ica.2006.07.074.

[46] A. Weibel, R. Bouchet, F. Boulc, P. Knauth, The big problem of small particles: a comparison of methods for determination of particle size in nanocrystalline anatase powders, Chem. Mater. 17 (2005) 2378–2385, https://doi.org/10.1021/cm0403762.

[47] M. Rabiei, A. Palevicius, A. Monshi, S. Nasiri, A. Vilkauskas, G. Janusas, Comparing methods for calculating nano crystal size of natural hydroxyapatite using x-ray diffraction, Nanomaterials 10 (2020) 1627, https://doi.org/10.3390/nano10091627.

[48] S.A. Disha, Md Sahadat Hossain, MdL. Habib, S. Ahmed, Calculation of crystallite sizes of pure and metals doped hydroxyapatite engaging Scherrer method, Halder-Wagner method, Williamson-Hall model, and size-strain plot, Results in Materials 21 (2024) 100496, https://doi.org/10.1016/j.rinma.2023.100496.

[49] S.C. Tjong, H. Chen, Nanocrystalline materials and coatings, Mater. Sci. Eng. R Rep. 45 (2004) 1–88, https://doi.org/10.1016/j.mser.2004.07.001.

[50] D. Nath, F. Singh, R. Das, X-ray diffraction analysis by Williamson-Hall, Halder-Wagner and size-strain plot methods of CdSe nanoparticles- a comparative study, Mater. Chem. Phys. 239 (2020) 122021, https://doi.org/10.1016/j.matchemphys.2019.122021.

[51] A.A. Akl, S.A. Mahmoud, S.M. AL-Shomar, A.S. Hassanien, Improving microstructural properties and minimizing crystal imperfections of nanocrystalline Cu 2 O thin films of different solution molarities for solar cell applications, Mater. Sci. Semicond. Process. 74 (2018) 183–192, https://doi.org/10.1016/j.mssp.2017.10.007.

[52] MdK. Alam, MdS. Hossain, N.M. Bahadur, S. Ahmed, A comparative study in estimating of crystallite sizes of synthesized and natural hydroxyapatites using Scherrer Method, Williamson-Hall model, Size-Strain Plot and Halder-Wagner Method, J. Mol. Struct. 1306 (2024) 137820, https://doi.org/10.1016/j.molstruc.2024.137820.

[53] V. Mote, Y. Purushotham, B. Dole, Williamson-Hall analysis in estimation of lattice strain in nanometer-sized ZnO particles, Journal of Theoretical and Applied Physics 6 (2012) 6, https://doi.org/10.1186/2251-7235-6-6.

[54] A.A. Akl, A.S. Hassanien, Comparative microstructural studies using different methods: effect of Cd-addition on crystallography, microstructural properties, and crystal imperfections of annealed nano-structural thin CdxZn1-xSe films, Physica B Condens Matter 620 (2021) 413267, https://doi.org/10.1016/j.physb.2021.413267.

[55] A.A. Akl, I.M. El Radaf, A.S. Hassanien, An extensive comparative study for microstructural properties and crystal imperfections of Novel sprayed Cu3SbSe3 Nanoparticle-thin films of different thicknesses, Optik 227 (2021) 165837, https://doi.org/10.1016/j.ijleo.2020.165837.

[56] P. Shunmuga Sundaram, T. Sangeetha, S. Rajakarthihan, R. Vijayalaksmi, A. Elangovan, G. Arivazhagan, XRD structural studies on cobalt doped zinc oxide nanoparticles synthesized by coprecipitation method: Williamson-Hall and size-strain plot approaches, Physica B Condens Matter 595 (2020) 412342, https://doi.org/10.1016/j.physb.2020.412342.

[57] L. Motevalizadeh, Z. Heidary, M.E. Abrishami, Facile template-free hydrothermal synthesis and microstrain measurement of ZnO nanorods, Bull. Mater. Sci. 37 (2014) 397–405, https://doi.org/10.1007/s12034-014-0676-z.

[58] A. Sa'aedi, A.A. Akl, A.S. Hassanien, Effective role of Rb doping in controlling the crystallization, crystal imperfections, and microstructural and morphological features of ZnO-NPs synthesized by the sol–gel approach, CrystEngComm 24 (2022) 4661–4678, https://doi.org/10.1039/D2CE00483F.

[59] A. Hepp, C. Baerlocher, Learned peak shape functions for powder diffraction data, Aust. J. Phys. 41 (1988) 229, https://doi.org/10.1071/PH880229.

[60] N.C. Halder, C.N.J. Wagner, Separation of particle size and lattice strain in integral breadth measurements, Acta Crystallogr. 20 (1966) 312–313, https://doi.org/10.1107/S0365110X66000628.

[61] D. Balzar, H. Ledbetter, Voigt-function modeling in Fourier analysis of size- and strain-broadened X-ray diffraction peaks, J. Appl. Crystallogr. 26 (1993) 97–103, https://doi.org/10.1107/S0021889892008987.

[62] M. Frasnelli, F. Cristofaro, V.M. Sglavo, S. Dirè, E. Callone, R. Ceccato, G. Bruni, A.I. Cornaglia, L. Visai, Synthesis and characterization of strontium-substituted hydroxyapatite nanoparticles for bone regeneration, Mater. Sci. Eng. C 71 (2017) 653–662, https://doi.org/10.1016/j.msec.2016.10.047.

[63] C.J. Harrison, P.V. Hatton, P. Gentile, C.A. Miller, Nanoscale strontium-substituted hydroxyapatite pastes and gels for bone tissue regeneration, Nanomaterials 11 (2021), https://doi.org/10.3390/nano11061611.

[64] Md Kawsar, MdS. Hossain, N.M. Bahadur, S. Ahmed, Synthesis of nano-crystallite hydroxyapatites in different media and a comparative study for estimation of crystallite size using Scherrer method, Halder-Wagner method size-strain plot, and Williamson-Hall model, Heliyon 10 (2024) e25347, https://doi.org/10.1016/j.heliyon.2024.e25347.

[65] M.H. Baradaran-Ghandi, S.A. Hassanzadeh-Tabrizi, Mechanochemical self-explosive synthesis and characterization of Mo-V2C nanocomposite, Ceram. Int. 44 (2018) 5447–5452, https://doi.org/10.1016/j.ceramint.2017.12.177.

[66] D.H. Manh, T.T. Ngoc Nha, L.T. Hong Phong, P.H. Nam, T.D. Thanh, P.T. Phong, Determination of the crystalline size of hexagonal La $_{1-x}$ Sr$_x$ MnO3 ($x = 0.3$) nanoparticles from X-ray diffraction – a comparative study, RSC Adv. 13 (2023) 25007–25017, https://doi.org/10.1039/D3RA04018F.

[67] K. Patel, A. Patel, V.P. Jethwa, H. Patel, G.K. Solanki, X-ray diffraction analysis of orthorhombic SnSe nanoparticles by Williamson–Hall, Halder–Wagner and Size–Strain plot methods, Chemical Physics Impact 8 (2024) 100547, https://doi.org/10.1016/j.chphi.2024.100547.

[68] N. Jahan Tamanna, Md Sahadat Hossain, N. Mohammed Bahadur, S. Ahmed, Green synthesis of Ag2O & facile synthesis of ZnO and characterization using FTIR, bandgap energy & XRD (Scherrer equation, Williamson-Hall, size-train plot, Monshi- Scherrer model), Results Chem 7 (2024) 101313, https://doi.org/10.1016/j.rechem.2024.101313.

[69] B. Himabindu, N.S.M.P. Latha Devi, B. Rajini Kanth, Microstructural parameters from X-ray peak profile analysis by Williamson-Hall models; A review, Mater Today Proc 47 (2021) 4891–4896, https://doi.org/10.1016/j.matpr.2021.06.256.

[70] P.Ch Dey, R. Das, Impact of silver doping on the crystalline size and intrinsic strain of MPA-capped CdTe nanocrystals: a study by Williamson–Hall method and size–strain plot method, J. Mater. Eng. Perform. 30 (2021) 652–660, https://doi.org/10.1007/s11665-020-05358-9.

[71] R. Wati, Y. Yusuf, Effect of sintering temperature on carbonated hydroxyapatite derived from common cockle shells (cerastodermaedule): composition and crystal characteristics, Key Eng. Mater. 818 (2019) 37–43, https://doi.org/10.4028/www.scientific.net/KEM.818.37.

[72] I.K. Januariyasa, Y. Yusuf, Carbonated hydroxyapatite derived from snail shells (*Pilla ampulacea*): the influence of sintering temperature on purity and crystallography properties, Mater. Sci. Forum 975 (2020) 82–87, https://doi.org/10.4028/www.scientific.net/MSF.975.82.

[73] V.N. Hegde, M V V, J. Lumbini, S. Shanika, S. R, Effect of calcination temperature on structural, morphological elastic and electrical properties of MgO nanoparticles synthesized by combustion method, J. Phys. Chem. Solid. 192 (2024) 112071, https://doi.org/10.1016/j.jpcs.2024.112071.